ORIGINAL PAPER

The decisive factor of hollow spherical network morphology of $Nd_{1-x}Ce_xCo_{1-y}Cu_yO_{3\pm\delta}$ perovskites towards soot oxidation

Hari Prasad Uppara[1] · Sunit Kumar Singh[2] · Nitin Kumar Labhsetwar[2] · Mudiyaru Subrahmanya Murari[3] · Harshini Dasari[1]

Abstract

The perovskites $Nd_{1-x}Ce_xCo_{1-y}Cu_yO_3$ ($x = 0$–0.05, $y = 0$–0.1) have been synthesized using PVP-assisted sol–gel method and applied for soot oxidation reactions. XRD technique reveals the formation of orthorhombic phase with crystal volume of around ~ 214 Å^3 and crystal size of ~ 25–40 nm. The interconnected nanoparticles with hollow spherical network morphology of particles are observed for the samples $NdCoO_3$ (NC1) and $Nd_{0.98}Ce_{0.02}Co_{0.95}Cu_{0.05}O_3$ (NC2) with particle sizes of around 300–500 nm. The samples experienced a charge transfer from ligand (O^{2-}) to cobalt cation in UV region (210–260 nm) and also observed broad absorption bands in the visible region (380–600 nm). In addition, the bandgap energy of NC2 showed the lowest value (4.21 eV); as well as surface morphological advantage promoted the transport of surface-chemisorbed oxygen species in the inner and outer surface of catalysts surface due to the reducibility of the catalyst with the soot $\left(\frac{O_2^{x-}}{O_2^{x-}+O^{2-}} = 0.90 \right)$. Furthermore, XPS results evidenced the higher content of Co^{2+} cation upon substitution of Ce/Cu into NC1, which successively formed more amount of O_β-oxygen species. Remarkably, the perovskite NC2 showed the lowest soot oxidation temperature ($T_{50\%} = 434$ °C) among the investigated perovskites. Besides, the spherically networked morphology of NC2/NC1 samples also decided the soot oxidation process.

Keywords Spherically networked morphology · Perovskite · $NdCoO_3$ · Soot oxidation · Bandgap energy

Introduction

The diesel combustion engines play a prominent role in heavy trucks and off-road vehicles. The technological advancements towards diesel engine modifications, particularly controlling the soot emissions from diesel engine exhaust, are under study and need to explore for commercial applicability (Adler 2005). Soot nanoparticles (≤ 2.5 μm), an airborne contaminant in the environment, undergo drastic changes in climatic conditions as well as affect the human's lifestyle. Recent years have witnessed tremendous research on the abatement of soot emissions. Many researchers have attempted different technology and methodology to bring down the soot emissions to a nominal level (Stanmore et al. 2001); however, it remains an open challenge to the scientific community.

Generally, the bare soot oxidizes in the temperature range of 590–650 °C. However, it is difficult to operate the diesel exhaust engine in that temperature range. Thus, to address this challenge, researchers proposed catalytic oxidation as one of the viable alternative techniques to lessen the soot oxidation temperature by arranging the catalysts at the diesel exhaust filter. The advancement of scientific knowledge in catalysis has strongly relied on gathering information about the surface, topological, and chemical properties. To overcome the current technical aspects of diesel engines by developing more catalytically active, which can drastically decrease the light-off temperatures for the soot oxidation reaction. Thus, researchers need to build a realistic model benefiting both societal as well as economic aspects. Moreover, the soot–catalyst mixture's interaction also plays one of

✉ Harshini Dasari
harshini.dasari@manipal.edu

1 Department of Chemical Engineering, Manipal Institute of Technology, Manipal Academy of Higher Education, Manipal 576104, India

2 Energy and Resource Management Division, CSIR-NEERI, Nagpur, Maharashtra, India

3 DST-PURSE Program, Mangalore University, Mangalagangotri 574199, India

the most critical factors, and it can achieve in two different modes, i.e. loose and tight contact. The ball milling of soot and catalyst under tight conditions gives better soot oxidation than under loose conditions. (Piumetti et al. 2016).

The researchers attempted many different catalysts like mixed oxides (Zhai et al. 2019), spinel-type of oxides, and perovskites (Uppara et al. 2019, 2020) towards soot oxidation applications. Perovskites, one among catalysts, exhibited good catalytic properties towards soot oxidation (Mishra and Prasad 2014). An intense research was already carried out with different structures of perovskites but still needs to explore few more interesting facts in an account of socio-economic benefits. Perovskites have recently attracted much attention because the tunable structure of perovskite material allows partial substitutions at A- and B-site cations with the other group of metals and reducible tendency causes the structural distortions/defects (Royer et al. 2014; Levasseur and Kaliaguine 2009), which in turn enhances the oxygen vacancies on the surface. Due to this fact, it can able to deliver active surface oxygen species (peroxides/superoxide's) to oxidize the soot at a lower temperature (Liu et al. 2016).

Wang et al. (2012) reported lanthanum cobaltite's ($T_m = 421$ °C) showed higher soot oxidation activity than lanthanum manganite's ($T_m = 448$ °C) and lanthanum ferrites ($T_m = 488$ °C). This was due to the good redox property of cobalt and the lower temperature reduction peaks promoted to generate more surface-adsorbed and lattice oxygen species. Li et al. (2010) studied $La_{0.9}K_{0.1}Co_{1-x}Fe_xO_3$ perovskite for NO_x assisted soot oxidation. They noticed that replacement of Co^{3+} by Fe^{3+} enhances the formation of Fe^{4+} cation and surface lattice oxygen species. Among the prepared samples, $La_{0.9}K_{0.1}Co_{0.9}Fe_{0.1}O_3$ showed higher soot oxidation activity with maximal soot combustion temperature obtained as 362 °C. Similarly, Co^{3+} substituted with Mg^{2+}, studied by Fang et al. (2014). They noticed that the sample $La_{0.6}K_{0.4}Co_{0.9}Mg_{0.1}O_3$ perovskite exhibited the T_m value as 359 °C under tight contact mode.

Furthermore, many research groups were attempted to synthesize the different morphologies of the perovskites to improve the catalytic activity. Feng et al. (2015, 2016, 2017) research group attempted to improve the soot oxidation activity by synthesizing the three dimensionally ordered macroporous (3DOM) perovskite using colloidal crystal template method. These 3DOM catalysts provide inner pores of the catalyst in which soot particles can able to penetrate into the pores without offering any resistance; thus, soot particles cover more surface contact points with the catalysts surface. They also examined that calcination temperature was one the most important factors to obtain the fine tubular nanoparticles. They fabricated $LaFeO_3$ and $LaCoO_3$ perovskites into nano-tubes (with K and Sr as dopants), tested for soot oxidation applications. The intrinsic catalytic activity

(reducibility properties and surface oxygen vacancies) was improved with the incorporation of certain K content; however, excessive K content led to destruction of nano-tubular structure. It was due to the formation of eutectics with the other components of the catalyst which might show negative catalytic properties. The introduction of K and Sr into the perovskite improved the NO_x storage capacity and also further enhanced the soot oxidation activity. Similarly, web structure 3D nano-fibres were synthesized by Lee et al. (2016). They reported that these 3D structure nano-fibres have high contact area because of large pores which can trap the soot particles into the unique surface morphology and it is effective for soot oxidation. The 3D nano-fibres of $La_{1-x}Sr_xCo_{0.2}Fe_{0.8}O_{3-\delta}$ ($T_{max, H} = 585$ °C) have shown higher soot oxidation activity than the of $La_{1-x}Sr_xCo_{0.2}Fe_{0.8}O_{3-\delta}$ bulk catalyst ($T_{max, H} = 623$ °C). Thus, the reported studies proved that catalyst surface morphology was playing prominent role for soot oxidation reactions.

With this literature evidence, we attempted to synthesize the unique surface morphological catalysts in order to improve the soot oxidation activity. In particularly, spherical network morphology of interconnected particles with the availability of voids on the surface was synthesized using PVP-assisted sol–gel method. In this study, $NdCoO_3$ perovskite was synthesized by incorporating the Ce at A site and Cu at B site, and studied its effect towards soot oxidation reactions.

In specifically, the compounds such as $NdCoO_3$, $Nd_{0.98}Ce_{0.02}Co_{0.95}Cu_{0.05}O_3$, $Nd_{0.98}Ce_{0.02}Co_{0.90}Cu_{0.10}O_3$, and $Nd_{0.95}Ce_{0.05}Co_{0.95}Cu_{0.05}O_3$ (henceforth referred as NC1, NC2, NC3, and NC4, respectively) were synthesized and tested its performance towards soot oxidation activity. To the best of our knowledge, the literature on Nd-based perovskites towards soot oxidation applications was limited.

Experimentation

Synthesis of $Nd_{1-x}Ce_xCo_{1-y}Cu_yO_3$ perovskites

The perovskites (NC1, NC2, NC3, and NC4) are synthesized using the PVP-assisted sol–gel method, as reported in our previous work (Uppara et al. 2021). To synthesize these samples, the following precursors are used: $Nd(NO_3)_3$ $6H_2O$ (crystals and lumps, 99.9% trace metals basis, Sigma-Aldrich), $Ce(NO_3)_3$ $6H_2O$ (99% trace metals basis, HIMEDIA), $Co(NO_3)_2.6H_2O$ ($\geq 98\%$, Merck), $Cu(NO_3)_2.3H_2O$ ($\geq 98\%$, Merck), citric acid monohydrate ($\geq 99\%$, Merck), polyvinylpyrrolidone (PVP, average MW ~ 1,300,000 by LS, Sigma-Aldrich). The required quantities of metal precursors (shown in Table 1) dissolved in 100 mL of deionized water under constant stirring for 1 h. It allowed dispersing the metals uniformly in the solution. In this solution, the

Table 1 The amount of metal nitrates used and the corresponding moles of metals used in the synthesis of perovskite

Sample	Nd		Ce		Co		Cu	
	Nd nitrate (g)	Moles of Nd metal	Ce nitrate (g)	Moles of Ce metal	Co nitrate (g)	Moles of Co metal	Cu nitrate (g)	Moles of Cu metal
NC1	3.49	0.008	–		2.31	0.008	–	
NC2	3.41	0.0077	0.069	0.00016	2.20	0.0075	0.096	0.0004
NC3	3.41	0.0077	0.069	0.00016	2.08	0.0071	0.192	0.0008
NC4	3.31	0.0004	0.172	0.0004	2.20	0.0004	0.096	0.0004

weight ratio (1.5:1) of metal nitrates and PVP was added slowly under constant stirring and allowed to mix uniformly with the solution. Subsequently, the combustible citric acid was added to the solution (citric acid/metals = 1.5/1). To the resultant solution, the aqueous ammonia solution (28% NH_3 solution) was added slowly and the pH of the solution was maintained at around 10. The resultant solution dried at 90 °C to form the gel, followed by combustion at 130 °C to form the hard substance. Finally, the hard material was grinded to fine particles and carried the calcination at 900 °C for 6 h. The schematic synthesis procedure of Nd-based perovskite is shown in Fig. 1.

Experimental details of characterization techniques

XRD analysis was performed on Rigaku X-ray diffractometer using Cu-Kα radiation ($\lambda = 1.54$ Å). The data were collected with 2° min^{-1} scanning rate from 20 to 80°. The crystal size of the as-synthesized perovskites was obtained by Debye–Scherrer equation. The images of surface morphology were captured using field emission scanning electroscope (FESEM) and the elements with their composition were examined using energy-dispersive X-ray spectroscopy (EDS). Fourier transform infrared spectroscopy (FTIR) technique is carried out using FT/IR-6300 (Jasco). Herein, the sample mixed with KBr and scanned in the range of 400–4000 cm^{-1} wavenumber with a scanning resolution of 0.07 cm^{-1}. UV–Visible diffuse reflectance spectrometer (UV–Vis DRS) was carried out using Perkin Elmer (Lambda
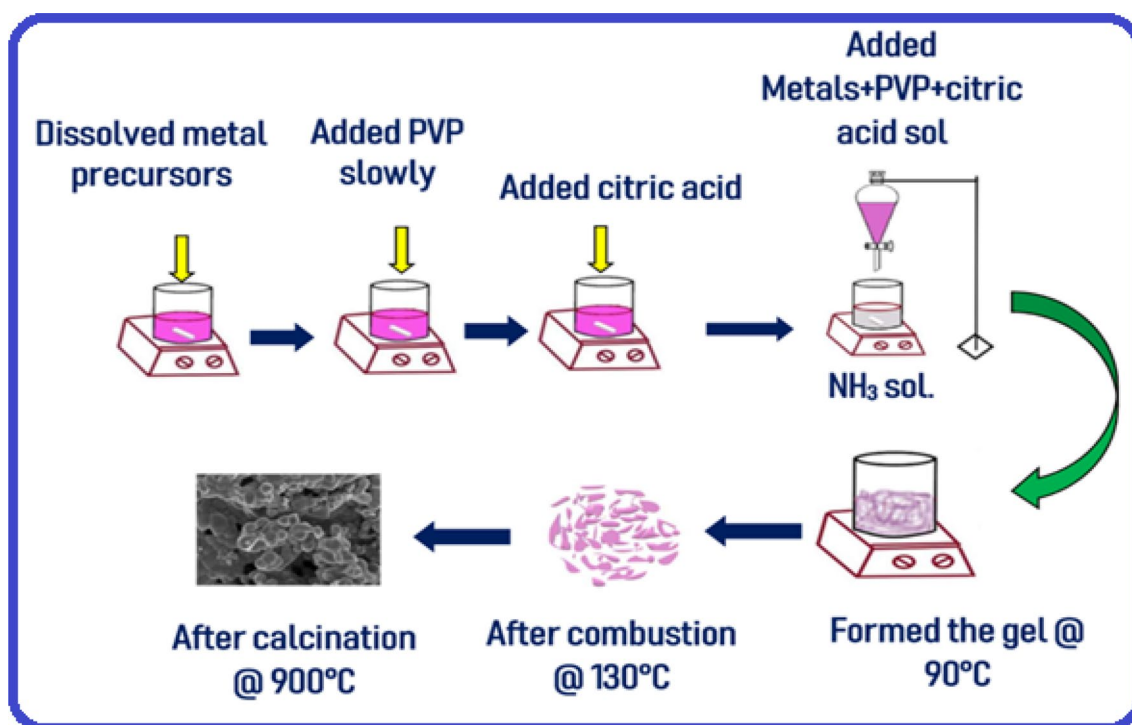
Fig. 1 Schematic synthesis procedure of Nd-based perovskites using PVP-assisted sol–gel method

950) in the wavelength range of 200–800 nm with an attachment of 150 mm integrating sphere diffuse reflectance.

X-ray photoelectron spectroscopy (XPS) studies were carried in Thermo Fisher Scientific (Model: K-Alpha) using Al Kα radiation; the binding energies were corrected with C1s peak at 284.8 eV. Soot–temperature-programmed reduction (Soot–TPR) experiments were conducted under the flow of inert gas, particularly, Argon gas (99.998%) with 60 mL. min^{-1} flow rate, to identify the reducible characteristics of the catalyst in the presence of soot under inert gas atmosphere. In this experiment, the soot–catalyst in the ratio of 1/10 was studied in the TGA instrument by ramp heating rate of 10 °C.min^{-1} in the temperature range of 50 °C–700 °C and the emitted CO_2 gas was recorded using CO/CO_2 analyser (NDIR sensor).

Catalyst performance studies

The catalytic performance of perovskites towards soot was examined in TA 55 instrument. Carbon black—Printex U (Degussa) with 20–50 nm-diameter range was used for soot oxidation experiments. For each experiment, 0.02 g of catalyst–soot mixture in the ratio of 10/1 was initially activated at 150 °C under an inert Argon gas flow (60 mL.min^{-1}). Then, the activated sample tested for soot oxidation experiments by measuring the weight loss of the mixture in the temperature range of 150–700 °C at 10 °C.min^{-1} under the

flow of 5% O_2 (N_2 balanced) gas. Then, the exhaust CO_2 gas was measured using ACCURA CO_2 analyser (NDIR sensor).

Results and discussion

X-ray diffraction technique (XRD)

XRD profiles of the as-synthesized perovskites are recorded at room temperature and shown in Fig. 2i and ii and the corresponding crystal parameters (crystal size, volume, lattice lengths, and strain) are calculated and displayed in Table 2. All the peaks were indexed to the orthorhombic phase (ICDD card no. 89-0551) and well matched with the literature (Ateia et al. 2019). The samples NC1 and NC2 exhibited a single phase of orthorhombic phase with a high degree of crystallinity. It is also noticed that the XRD pattern of the doped perovskite (NC2) did not modify the parent structure of $NdCoO_3$. The main diffraction peaks of the sample NC2, i.e. simultaneously doping A site (2 mol% Ce^{4+}) and B site (5 mol% Cu^{2+}) in $NdCoO_3$ perovskite, shifted the main peak towards higher 2θ angles as shown in the enlarged Fig. 2ii. This is related to lattice contraction of the orthorhombic phase of the perovskite (a decrease in crystal volume and crystal size is observed as shown in Table 2). The lattice contraction greatly impacted due to the substitution of smaller cation Co^{3+} (0.61 Å) with the larger cations Cu^{2+} (0.73 Å), however, less impacted with the substitution
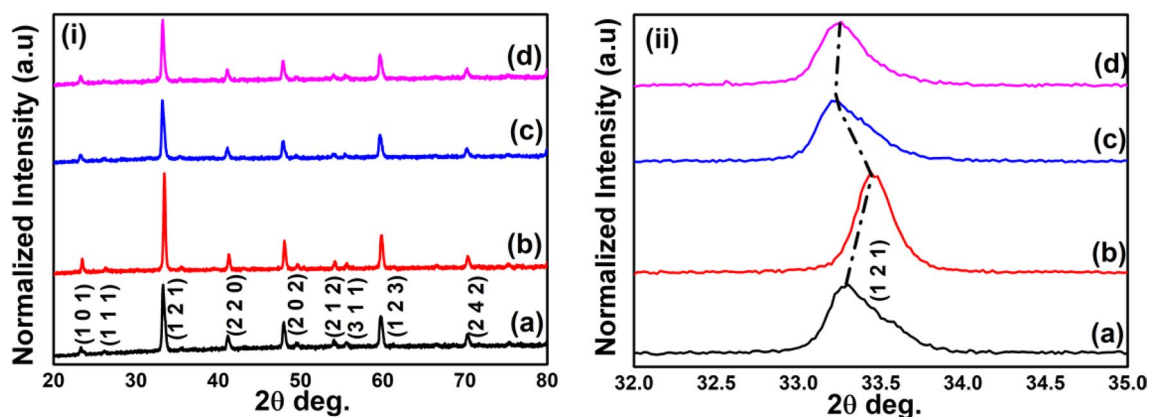

Fig. 2 XRD profiles of the samples **a** NC1 **b** NC2 **c** NC3, and **d** NC4

Table 2 Crystal size, crystal volume and lattice parameters of the as-synthesized perovskites

S. no	Sample	2θ (121)	Lattice parameters (Å)			Crystal volume (Å^3)	Crystal size (nm)	Lattice strain
			a	b	c			
1	NC1	33.282	5.269	7.769	5.233	214.24	36.5	0.00327
2	NC2	33.409	5.263	7.761	5.219	213.24	34.0	0.00349
3	NC3	33.208	5.287	7.769	5.230	214.88	39.0	0.00307
4	NC4	33.179	5.287	7.751	5.241	214.83	25.9	0.00463

of Nd^{3+} (1.109 Å) with Ce^{4+} (0.97 Å) because of the lower content of ceria (Urán et al. 2020; Schön et al. 2017). It can also be seen in Table 2 that the NC2 sample exerted more lattice strain upon doping Ce^{4+}/Cu^{2+} into $NdCoO_3$ perovskite, confirming the successful incorporation of dopants into pure perovskite. As reported in the literature (Cui et al. 2019), the successful dopant incorporation promotes lattice shrinkage which successively induces the structural defects (creation of oxygen vacancies) to counterbalance the charge compensation in the structure. Thus, the as-synthesized perovskite structures might also provide structural defects, but it can further confirm using FTIR analysis.

In NC3 sample, the dopant composition of Cu^{2+} at B site increases from 5 to 10 mol% by keeping Ce^{4+} as 2 mol% at A site. Similarly, in the NC4 sample, the composition of Ce^{4+} at A site increases from 2 to 5 mol% by keeping Cu^{2+} as 5 mol% at B site. In both the samples (NC3 and NC4), the main diffraction peak shifted towards lower 2θ angles when compared with NC1 and NC2 as shown in Fig. 2ii. It indicates that there might be a phase transition that occurs with the further increase in composition in both sites; moreover, the intensity of the main diffraction peak tremendously decreased implying that there is a drastic decrease in the degree of crystallinity. These peak shifts in XRD patterns of prepared samples indicate that increase in the percentage of dopants results in inefficient substitution of Nd/Co with Ce/Cu (as indicated by XRD of NC3 and NC4 compared to NC2). Hence, Cu is present as nanocrystalline or amorphous CuO supported over $NdCoO_3$ perovskite. This is also supported by EDS results.

FESEM/EDS analysis

Figure 3 depicts the morphology and elemental composition of the as-synthesized perovskites. For the samples NC1 and NC2, it evidenced the formation of nanoparticle morphology with particles that are interconnected each other and form like a spherical network, with the formation of voids in between the particles, shown in magnified Fig. 3. However, after doping higher content of Ce/Cu into the perovskites (NC3 and NC4) disappeared the network-like morphology and forms the smaller agglomerated nanoparticles. Moreover, the particles of all the samples possess a size around 300–500 nm, which is much higher than the size of soot nanoparticles (50–100 nm) (Guo et al. 2013). Herein, the size ratio of as-synthesized perovskites to soot particles is in the range of 5–6. It is worth noting that the size ratio must be greater than one in order to provide more surface contact of the catalyst with the soot particles. Thus, as-synthesized samples exhibit higher size-ratio value, providing more contact points with the soot particles. Besides, NC1 and NC2 samples possess a more morphological advantage over NC3 and NC4 samples in which the soot nanoparticles can able to

penetrate through the voids and are trapped inside the hollow spherical morphology providing both inner and outer surface contact points with the soot. The composition of elements Nd, Ce, Co, Cu is shown in Table 3, which confirms the presence of all the elements. The elemental composition obtained from EDS is lower than the nominal composition due to experimental loss.

Fourier transform infrared spectroscopy (FTIR)

The perovskites (ABO_3) have B–O bonds of BO_6 octahedron units and 12-coordinated A–O units. Wang et al. (2010) found that BO_6 octahedron units are stronger than Ln–O bonds in the spectroscopic behaviour. Among the six infrared vibrations of the octahedron, only the $\nu3$ and $\nu4$ modes are active. In specifically, $\nu3$ infrared mode is related to stretching mode of B–O bond which usually occurs at the higher wavenumbers. Similarly, $\nu4$ infrared mode is corresponded to bending mode of B–O bond which occurs at lower wavenumber (Wang et al. 2010, 2012).

Figure 4i shows full-range FTIR spectra of the doped and the un-doped $NdCoO_3$ perovskites, while the FTIR spectrum in the range 400–1000 cm^{-1} is shown in Fig. 4ii. As reported by Fang et al. (2014), for $La_{1-x}Ce_xFe_{1-y}Co_yO_3$ perovskites two main absorption bands were observed at around 400 and 600 cm^{-1}, which corresponds to deformation vibration of O-Fe–O or O–Co–O and stretching vibration of Fe–O or Co–O, respectively. Similarly, in the present work, particularly the NC1 sample showed that vibration bands at around 472 and 584 cm^{-1} are related to bending vibration (O–Co–O) and stretching vibrations (Co–O), respectively. However, the doped samples (NC2, NC3, and NC4) showed that higher band wavenumbers at around ~570 cm^{-1} and the shoulder band at ~600 cm^{-1} are attributed to two kinds of stretching vibration of Co–O or Cu–O in BO_6 octahedron in the perovskite structure and the lower band observed at ~470 cm^{-1} is related to bending vibration of O–Co–O or O–Cu–O in the perovskite (Fang et al. 2014; Li et al. 2012; Wang et al. 2008). These absorption bands demonstrate the formation of ABO_3 perovskite structure with or without dopants as well as promoted the structural defects in the perovskite structure. Besides, for NC1 and NC2 samples, the weak bands observed at around ~1050–1100 and 1480 cm^{-1} (shown in Fig. 4i) are related to symmetric and asymmetric stretching vibrations of surface carbonate species. However, these peaks are disappeared in NC3/NC4 samples as the dopant composition increases. The reported studies (Liu et al. 2019) reveal that the presence of water molecules in the samples is essentially required for diesel soot exhaust applications; however, it promotes the soot oxidation process but it may damage the surface structure due to the presence of water molecules. Generally, the water molecules present on the surface because of exposure of
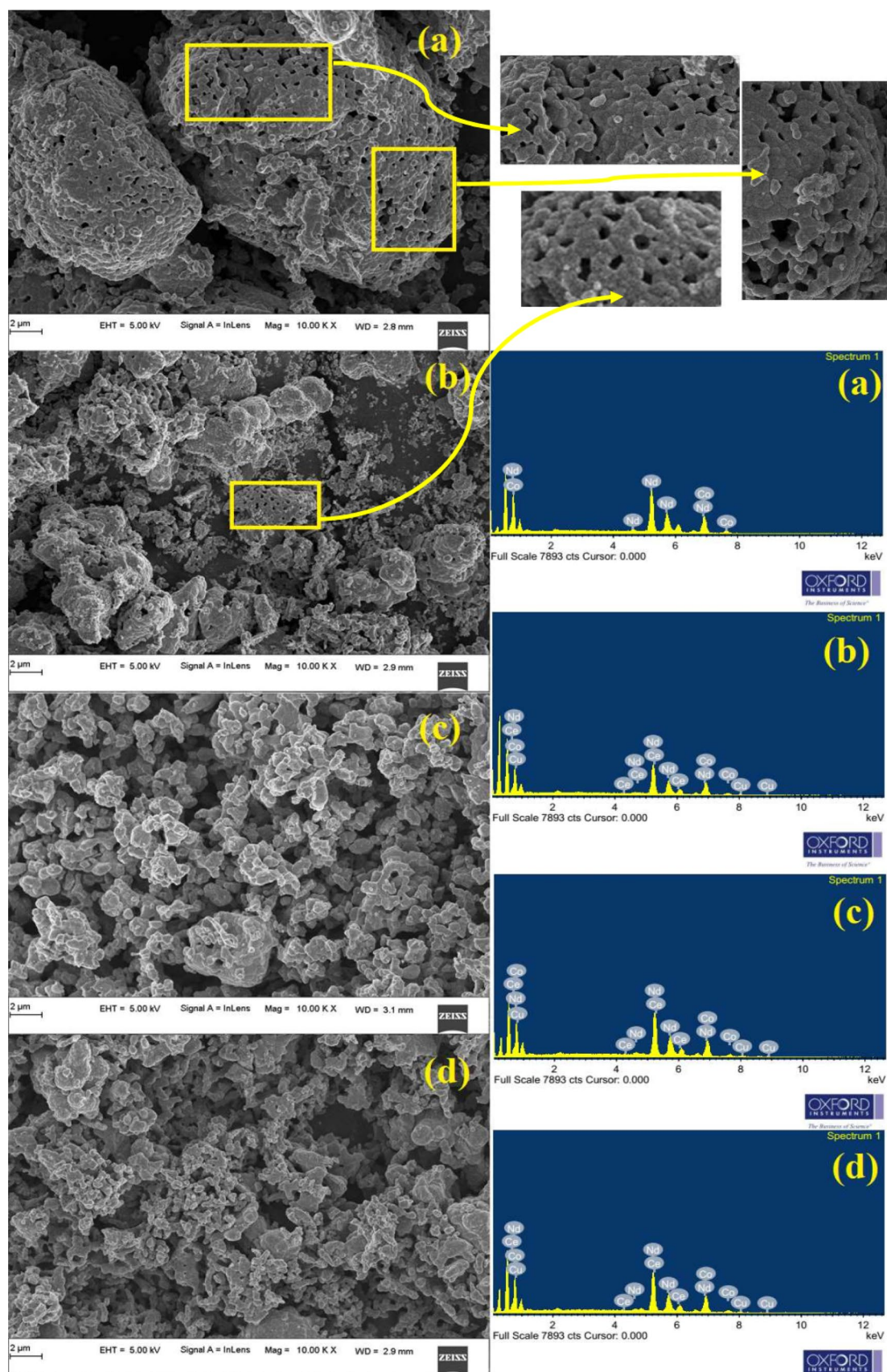
Fig. 3 FESEM/EDS images of the perovskites **a** NC1 **b** NC2 **c** NC3, and **d** NC4

**Table 3** Elemental composition of the perovskites from EDS technique

S. no	Sample	Elements	Theoretical composition	Composition from EDS
1	NC1	Nd/Co	0.5/0.5	0.44:0.56
2	NC2	Nd/Ce/Co/Cu	0.98/0.02/0.05/0.05	0.981/0.018/0.961/0.038
3	NC3	Nd/Ce/Co/Cu	0.98/0.02/0.9/0.1	0.979/0.020/0.932/0.067
4	NC4	Nd/Ce/Co/Cu	0.95/0.05/0.95/0.05	0.947/0.052/0.983/0.016
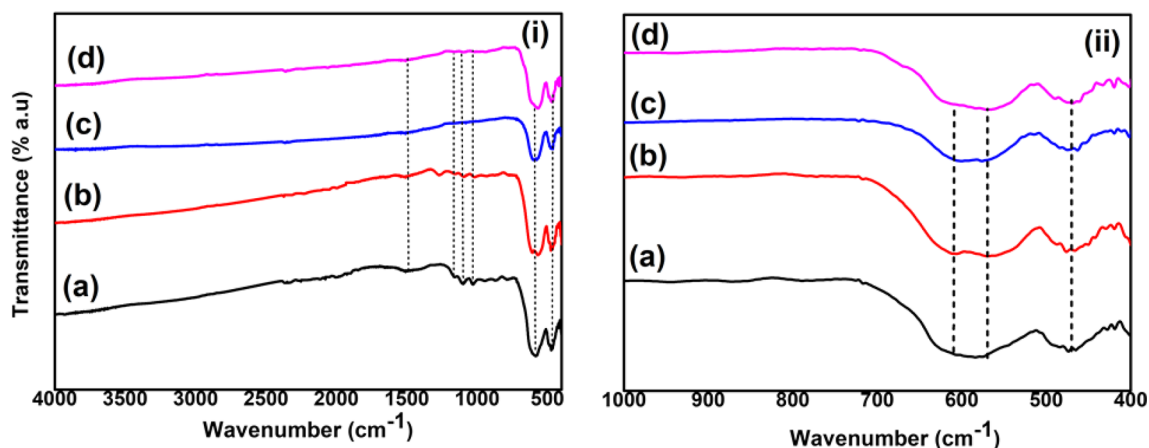
Fig. 4 i Full-range FTIR spectrum. **ii** FTIR spectrum in the range 400–1000 cm^{-1} of the samples **a** NC1 **b** NC2 **c** NC3, and **d** NC4

samples to air or environmental humidity and it exerts bands at around ~1600 and ~3450 cm^{-1} as reported in the literature (Liu et al. 2019; Basu and Ghosh 2013). However, there are no such bands observed in the present work. Interestingly, the capping agent (PVP) bands are also not observed in the spectra because the samples are calcined at 900 °C. As reported in the literature (Koczkur et al. 2015; Safo et al. 2019), the pure PVP bands that could be observed at around 1280, 1640, 2900 cm^{-1} are attributed to C–N bending vibration from pyrrolidone group, C=O stretching vibration of pyrrolidone structure, and CH stretching vibration, respectively. Interestingly, the capping agent (PVP) bands are also not observed in the spectra because the samples are calcined at 900 °C. In addition, the reported studies also reveal that the PVP agent should be removed before any catalytic reactions. This is due to the fact that the presence of these agents might block the active sites and hampers the mass transfer of reactants and the products (Han et al. 2020). Thus, it confirms the removal of PVP agent using this technique.

UV–Vis diffuse reflectance spectroscopy (UV–Vis DRS)

Figure 5 depicts the absorption bands identified in UV–Vis DRS of the as-synthesized perovskites, measured in the wavelength range of 200–800 nm. UV–Vis DRS spectra showed the presence of sharp absorption bands at around 200–300 nm in the UV region and broad bands in the
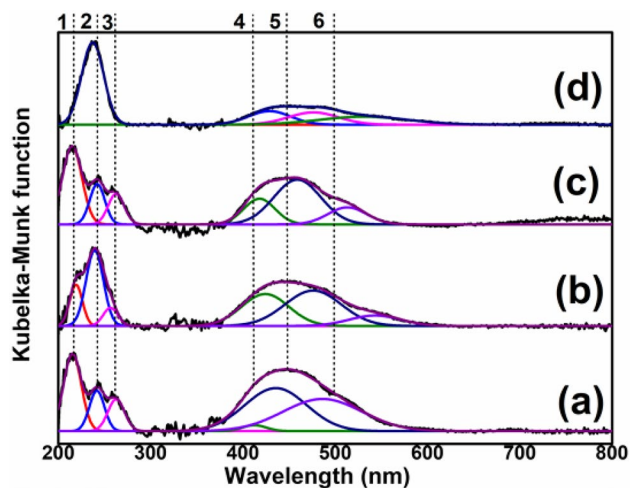
Fig. 5 UV–Vis DRS of the as-synthesized perovskites **a** NC1 **b** NC2 **c** NC4, and **d** NC3 [Note: 1–3 peaks belong to absorption bands in UV region and 4–6 peaks are absorption bands in visible region]

visible region 380–600 nm. These bands are consistent well with the reported literature, especially Liu et al. (2009) observed ligand-to-metal charge transfer in UV region and d-d transition bands in the visible region for the sample La$_{0.9}$K$_{0.1}$CoO$_3$/CeO$_2$. Similarly, in this study, all the peaks are fitted with Gaussian curves as shown in Fig. 5, which are attributed to the different excitation states of cobalt cation; however, the excitation states of dopants Ce/Cu are

not observed significantly because of lower atomic content. In this study, the perovskites exerted Co^{3+} (valence electrons = 6) and Co^{2+} (valence electrons = 7) cations on the surface of materials.

The doping of cerium and copper into $NdCoO_3$ greatly impacted the absorption bands. In the perovskites (NC1, NC2, and NC4), the absorption of UV radiation excites an electron from the lone pair orbitals of O2p at around ~216–220 nm and transfers to Co^{2+} ($O^{2-} \rightarrow Co^{2+}$) indicating ligand-to-metal charge transfer (LMCT). Similarly, the band at ~240 nm was attributed to charge transfer from O2p to Co^{3+}. In addition, the inter-band transition was also observed at around ~260 nm related to the excitation of an electron from one energy level to another level of Co^{2+} or Co^{3+}. However, NC3 exhibited only one absorption band

in the UV region at around 237 nm related to $O^{2-} \rightarrow Co^{3+}$ charge transfer transition. To understand the excitation process clearly, the excitation of electrons from O2p to cobalt cation upon absorption of UV radiation is schematically shown in Fig. 6. Here, the Co^{2+} conduction band was located at a higher energy position/lower wavelength than Co^{3+}. In addition, the crystal field of octahedral Co3d split into two levels: lower energy orbitals d_{xy}, d_{xz}, d_{yz} (denoted as t_{2g}) and the higher energy orbitals of $d_{x^2-y^2}$, d_z^2 (denoted as e_g).

The broad absorption band is also observed for all the samples in the visible region at around ~380–600 nm due to d-d electron transferring, indicating that the samples are responsive to the visible range; however, the peaks are slightly attenuated as it increases the dopants (Ce/

Fig. 6 The crystal field of octahedral Co3d and its corresponding excitation upon UV absorption of the samples **a** NC1 **b** NC2 **c** NC3, and **d** NC4
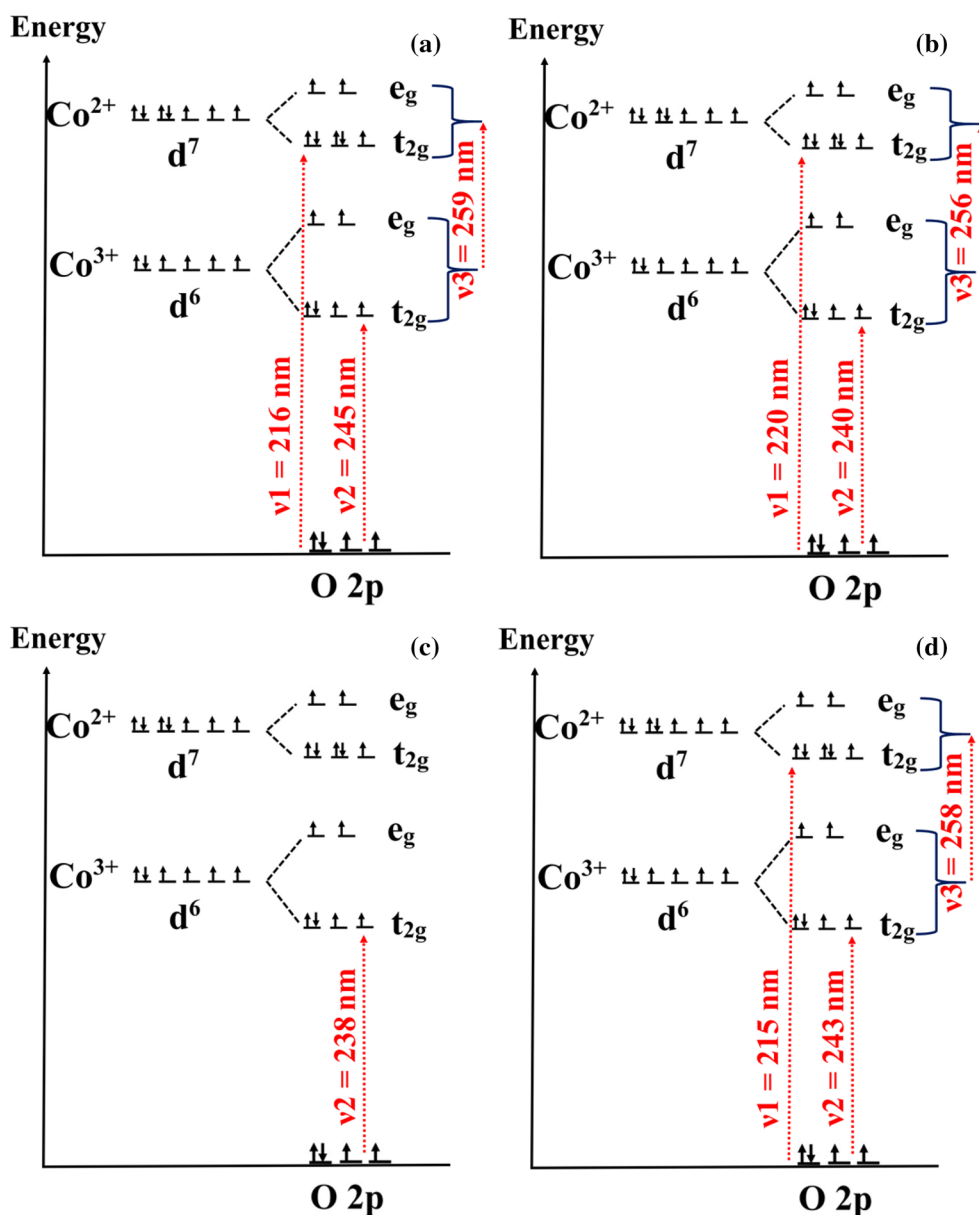
Cu) composition. The broad absorption bands in the visible region are deconvoluted into three peaks as shown in Fig. 5. The peaks (4–5) are related to $^4T_{1g} \rightarrow {}^4T_{1g}(P)$ and $^4T_{1g} \rightarrow {}^4T_{2g}$ transitions of Co^{2+} and the band (peak 6) is attributed to $^5T_{2g} \rightarrow {}^5E_g$ transition of Co^{3+}. Thus, all the samples exhibited the presence of Co^{2+} and Co^{3+} ions. Besides, the ratio of Co^{2+} to Co^{3+} was also calculated by the area under the curves (peaks 4–6 of Fig. 5) and corresponding ratios are shown in Table 4. This ratio signifies that all the doped samples (NC2, NC3, and NC4) consist of higher availability of Co^{2+} cations than Co^{3+}, because of the creation of lattice distortions, as already discussed in FTIR.

The bandgap energies of the samples are calculated using the Tauc plot as shown in Fig. 7. The Tauc equation is shown in Eqs. (1–2) (Murugan et al. 2005; Wang et al. 2020).

$$\left[F(R_\infty)h\nu\right]^{\frac{1}{n}} = C(h\nu - E_g) \tag{1}$$

$$F(R_\infty) = \frac{(1 - R_\infty)^2}{2R_\infty} \tag{2}$$

Herein, $F(R_\infty)$, R_∞, h, E_g, ν, C, n represent Kubelka–Munk function, diffuse reflectance, Planck's constant, incident light frequency, bandgap energy, a constant, and an integer. The integer "n" is chosen as 0.5 for the bandgap is in direct transition. It is observed that a plot between $\left[F(R_\infty)h\nu\right]^2$ and $h\nu$ was linear near the edge for the direct transition. The extrapolation of the straight line to abscissa provides information about bandgap energy. The calculated band gap energies for the direct transition are displayed in Table 4. The estimated bandgap energies of the samples NC1, NC2, NC3, and NC4 are 4.57, 4.21, 4.72, and 4.66 eV, respectively.

As reported by Getsoian et al. (2014), bandgap energy is the descriptor for catalytic propene oxidation reactions. Besides, it is reported that the samples exhibiting lower bandgap energies exhibit lower soot oxidation temperatures. It is because the materials can easily transfer an electron from ligand to metal and indirectly signifies that the material might possess a higher chance of migration of oxygen
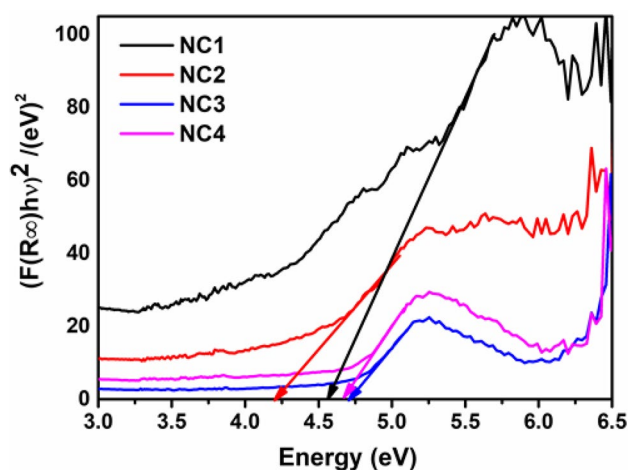

Fig. 7 The Tauc plots of the as-synthesized perovskites

species within the material. In this work, it is noticed that bandgap energies for NC2 are lower than the samples NC1, NC3, and NC4. Thus, the perovskite NC2 is potential candidate for oxidation reactions.

XPS analysis

XPS spectra of Co2p are shown in Fig. 8i. The peaks of Co2p of the perovskite NC1, centred at around 779.9 and 781.7 eV, are ascribed to Co^{3+} $2p_{3/2}$ and Co^{2+} $2p_{3/2}$, respectively, with spin–orbital contribution identified at around trivalent $Co2p_{1/2}$ (794.8 eV) and divalent Co $2p_{1/2}$ (796.5 eV). However, after incorporation of Ce/Cu cations in $NdCoO_3$, the binding energies (B.E) are shifted towards the lower value because of substitution of less electronegative element (Co—1.88) by the more electronegative (Cu—1.90) element. Thus, it confirms that the formation of Co^{2+} and Co^{3+} cations at B site induces the shift in B.E. In addition, the weak satellite peaks of Co2p are also observed at around ~790 eV and ~805 eV for all the samples with a spin–orbit energy difference of Co2p obtained as 14.5–15 eV. The binding energies in this study are consistent with the reported literature; in particular, Tsai et al. (2020) reported Co^{3+} (780.2,

Table 4 The wavelengths and bandgap energies of the as-synthesized perovskites

S. no	Sample	Wavelength (nm)						$^aCo^{2+}/Co^{3+}$ ratio	Band gap energy (eV)
		UV region			$^4T_{1g} \rightarrow {}^4T_{1g}(P)$	$^4T_{1g} \rightarrow {}^4T_{2g}$	$^5T_{2g} \rightarrow {}^5E_g$		E_g
1	NC1	216	245	259	413	435	492	1.1	4.57
2	NC2	220	240	256	424	480	550	6.5	4.21
3	NC4	215	243	258	418	461	516	4.4	4.66
4	NC3	–	238	–	425	477	539	1.7	4.72

^{a}The ratio of Co^{2+} to Co^{3+} is calculated from the area under the peaks in the visible region
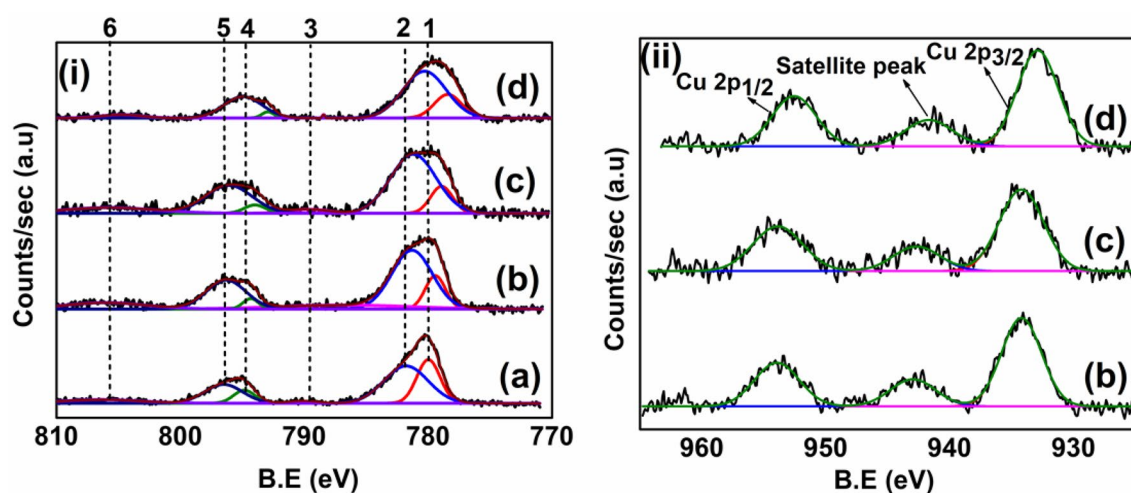
Fig. 8 XPS of Co2p **i** and Cu2p **ii** of the samples **a** NC1 **b** NC2 **c** NC3, and **d** NC4. [Note: 1—Co (III) $2p_{3/2}$, 2—Co (II) $2p_{3/2}$, 3—satellite peak, 4—Co (III) $2p_{1/2}$, 5—Co (II) $2p_{1/2}$, and 6—satellite peak]

795.1 eV) and Co^{2+} (781.8, 796.9 eV) cations on the surface of the MOF derived Co_3O_4 nanoparticles. Furthermore, the ratio's Co^{2+}/Co^{3+} for the samples NC1, NC2, NC3, and NC4 are obtained as 1.83, 4.20, 5.13, and 3.94, respectively. It infers that the ratio is higher than one, indicating that all the samples exhibit higher content of Co^{2+} cation than Co^{3+}. Further Cu2p peaks are deconvoluted into three, as shown in Fig. 8ii. The peaks located at around 934.2 and 953.9 eV are corresponded to Cu^{2+} $2p_{3/2}$ and Cu^{2+} $2p_{1/2}$, respectively. In addition, the satellite peak was also observed at around 942.9 eV. Thus, it affirms that all the samples provide Cu^{2+} cation on the surface with spin–orbital energy difference obtained as 19.7 eV. The obtained Cu2p peaks are consistent with the reported literature, i.e. Venkataswamy et al. (2019) reported Cu^{2+} peaks at 934.2 eV and 954.1 eV with spin–orbit energy difference obtained as 19.9 eV.

The substitution of Nd^{3+} by Ce^{4+} does not impact much on charge neutrality phenomena because of the lower content incorporation of Ce^{4+}. However, at the B site of perovskite, i.e. replacing cobalt cation with copper cation strongly influences the electronic neutrality because of the availability of $Co^{3+}/Co^{2+}/Cu^{2+}$ cations which successively generates the oxygen vacancies in order to compensate the charge neutrality.

O1s analysis

Figure 9 depicts O1s spectra of as-synthesized perovskites. The peaks are deconvoluted into three by fitting the peaks using the Gaussian function. The peaks identified at around 528 ± 0.7, 530 ± 0.8, and 532 ± 0.8 are attributed to lattice oxygen species (O_{α}), surface-chemisorbed oxygen (O_{β}), and hydroxyl/carbonate species (O_{γ}), respectively. It can be noticed from Fig. 9 that the peaks (O_{α} and O_{β}) of Ce/
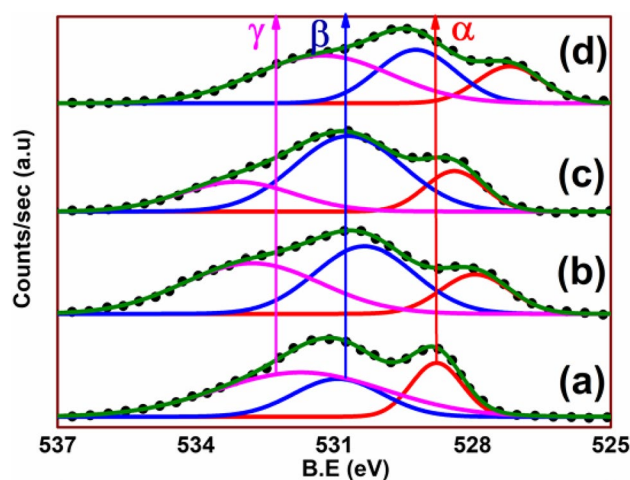
Fig. 9 The O1s spectra of the as-prepared perovskites **a** NC1 **b** NC2 **c** NC3, and **d** NC4

Cu incorporated samples are shifted towards lower binding energy as compared with NC1, which signifies that the interaction of Co/Cu cations successfully generates the oxygen vacancy sites on the surface of perovskites to maintain the charge balance. According to reported studies (Sun et al. 2020), surface-chemisorbed oxygen species (O_{β}) are electrophilic and are active during oxidation reactions. Indeed, more content of surface-adsorbed oxygen species (O_{β}) signifies the higher catalytic activity. Comparing with $NdCoO_3$ perovskite, the substitution of Ce/Cu cation increased the relative content of O_{β}-species. It can be seen from Table 5 that the ratio $O_{\beta}/(O_{\alpha} + O_{\beta} + O_{\gamma})$ of NC2 was found to be 0.587, which was 2.36, 1.43, and 1.82 times higher than NC1, NC3, and NC4, respectively. It infers that NC2 sample exhibits higher mobility of surface-chemisorbed oxygen

Table 5 The different oxygen species and corresponding binding energies examined using XPS O1s analysis

S. no	Sample	Elements	Peak position (eV)	FWHM	Area	$\frac{O_\beta + O_\gamma}{O_\alpha}$ ratio	$\frac{O_\beta}{(O_\alpha + O_\beta + O_\gamma)}$ ratio
1	NC1	O_L (α)	528.8	1.302	18,167.48	3.94	0.248
		O_{ads} (β)	530.9	2.268	22,273.31		
		O_{hyd} (γ)	531.7	4.313	49,482.78		
2	NC2	O_L (α)	528.4	1.513	15,889.02	4.81	0.587
		O_{ads} (β)	530.7	2.768	54,230.13		
		O_{hyd} (γ)	533.1	2.907	22,341.61		
3	NC3	O_L (α)	527.9	1.768	13,735.73	5.00	0.408
		O_{ads} (β)	530.3	2.537	33,651.63		
		O_{hyd} (γ)	532.8	3.521	35,130.98		
4	NC4	O_L (α)	527.2	1.666	20,741.31	4.46	0.320
		O_{ads} (β)	529.2	2.015	36,309.13		
		O_{hyd} (γ)	531.2	3.493	56,227.93		

species because of the higher content of O_β-species as well as overall oxygen species.

In addition, the parameter $(O_\beta + O_\gamma)/O_\alpha$ ratio is also defined to measure the performance of catalytic activity in terms of oxygen storage capacity (OSC) of the as-synthesized perovskites. According to the literature (Xiong et al. 2021), the species (O_β and O_γ) are usually adsorbed on the oxygen vacancy sites, which circuitously provides information about oxygen storage capacity. Interestingly, the $(O_\beta + O_\gamma)/O_\alpha$ ratio of the NC3 sample is obtained as 5.00 which was higher than NC2 (4.81), NC4 (4.46), and NC1 (3.94). It confirms the higher availability of oxygen vacancy density of the samples is as follows: NC3 > NC2 > NC4 > NC1. Herein, the higher oxygen vacancy concentration in the NC3 sample can be interpreted by comparing the amount of individual oxygen species of NC3 and NC2 samples. It can be noticed from Table 5 that the amount of O_γ-species in the NC3 sample was higher than NC2. However, the O_α-species are lower amount than NC2. Although, NC2 carries higher mobility of O_β-species but exhibits lower oxygen vacancy density than NC3. It is because the surface morphology of the catalysts also plays a role in creating surface oxygen vacancies. It signifies that NC2 sample limits the generation of vacancies because of spherical network particles in which inner and outer surfaces with narrow voids are available for utilization. However, in the NC3 sample, all the particles are separated individually and can easily penetrate the oxygen species, which can boost to create more vacancies as compared with NC2. Thus, the NC3 sample has higher oxygen vacancy concentration $((O_\beta + O_\gamma)/O_\alpha)$. However, NC2 possesses higher mobility of surface-chemisorbed oxygen species $(O_\beta/(O_\alpha + O_\beta + O_\gamma))$. Nonetheless, the catalytic performance of these catalysts is further confirmed using oxidation experiments.

Thus, the higher concentration of Co^{2+} and β-species in the doped samples suggests the generation of higher oxygen vacancy concentration because of substitution of Co by Cu cations. Among the as-synthesized samples, NC2 or NC3 might exhibit higher performance towards the oxidation reactions.

Soot-TPR analysis

Figure 10i displays that the soot-TPR analysis of the as-synthesized perovskites and the corresponding deconvolution of peaks are shown in Fig. 10ii. This analysis helps to investigate the role of different oxygen species involved during the oxidation process. The oxygen species evolved from the surface of perovskites was due to structurally deformed perovskites. There are two different mobile oxygen species released from the catalyst surface due to the surface reducible tendency of the catalysts. (i) Lower-temperature oxygen species (surface-adsorbed oxygen) evolved in the temperature range of 200–500 °C, represented as O_2^{x-}, these species are weakly bonded to the surface and actively participate in chemical reactions. (ii) Higher-temperature oxygen species (lattice oxygen) released at above 500 °C denoted as O^{2-} (Uppara et al. 2019, 2020), these species are difficult to release from the catalyst (Xiong et al. 2021). The peaks are distinguished (shown in Fig. 10ii) and estimated the peak areas by fitting the peaks using the Gaussian function. Then, the calculated amount of surface-adsorbed oxygen species (< 500 °C) and lattice oxygen species (> 500 °C) and the corresponding surface-adsorbed peak temperatures are displayed in Table 6. In particular, the low-temperature mobility of oxygen species (O_2^{x-}) plays a crucial role to initiate the soot oxidation process. The doped perovskite NC2 exhibited more amount of surface-chemisorbed oxygen species $\left(\frac{O_2^{x-}}{O_2^{x-} + O^{2-}} = 0.90\right)$ as compared with NC1. The soot-TPR analysis is well corroborated with XPS results, especially surface-chemisorbed oxygen O_β-species showed higher

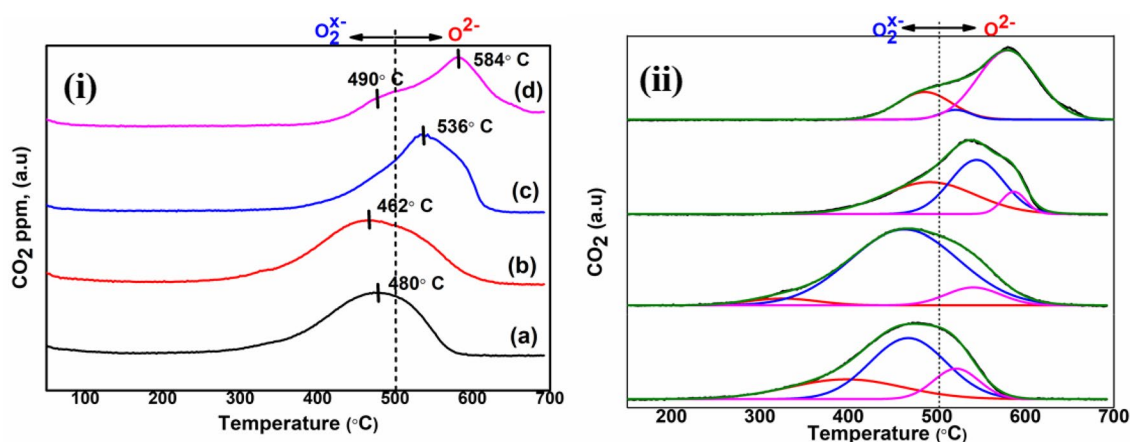**Fig. 10** Soot-TPR analysis of the samples **a** NC1 **b** NC2 **c** NC3, and **d** NC4

Table 6 Soot oxidation temperatures and active oxygen peak species of the as-synthesized perovskites

S. no	Sample	T_{ig} (°C)	T_{max} (°C)	$T_{50\%}$ (°C)	T_f (°C)	$T_{gap} = T_{ig} - T_f$	Soot-TPR T_{peak}	$\frac{O_2^{x-}}{(O_2^{x-} + O^{2-})}$
1	NC1	375	471	460	570	195	480	0.83
2	NC2	360	446	434	525	165	462	0.90
3	NC3	440	517	510	565	125	536	0.46
4	NC4	460	506	503	575	115	584	0.25

content for NC2 sample. Nonetheless, the other two samples NC3 and NC4 evidenced less amount of O_2^{x-} (< 50%) and the more pronounced quantity of lattice oxygen species (O^{2-}) which are not motivated for soot oxidation studies. The amount of surface-adsorbed oxygen species are in the order of NC2 > NC1 > NC3 > NC4. Thus, the perovskites NC2 might show superior soot oxidation activity as compared with the other perovskites.

Catalyst performance studies—"Possible Mechanism"

To evaluate the performance of the as-synthesized perovskites, the soot and the perovskites are mixed in the ratio of 1:10 under tight contact and carried the experiments under the flow of 5% O_2 (balance N_2). The performance of the perovskites towards soot oxidation is displayed in Fig. 11. In this experiment, $T_{50\%}$ (the temperature at which 50% of soot converted) and T_{max} (the temperature at which soot oxidation rate was maximum) were considered as the parameters to investigate the performance of catalysts towards soot oxidation and the corresponding values shown in Table 6. The $T_{50\%}$ conversion temperature of the samples NC1, NC2, NC3, and NC4 is measured as 460, 434, 510, and 503 °C, respectively.

Initially, the blank studies, i.e. un-catalysed soot oxidation experiments under O_2 flow, are investigated and noticed that the bare soot ignites at around 540 °C and completes its oxidation at around 660 °C. Indeed, the catalyst–soot mixture experiments are investigated under the same experimental conditions. It is worth noticing a shift in oxidation temperature to the lower region observed for catalysed soot oxidation experiments. It is because of some essential characteristic features of the as-synthesized perovskites like surface-chemisorbed oxygen species, redox property, and surface morphological changes that tend to enhance its activity.

In the NC1 sample, the soot combustion process starts to ignite at around 375 °C and completes its oxidation at around 570 °C. Although the maximum soot combustion of NC1 is shown at 471 °C, the complete conversion occurs at higher temperatures. It indicates the temperature gap between the ignition and the complete oxidation is around 195 °C, signifying that NC1 sample slowly oxidizes the soot during its combustion process. It is due to the fact that NC1 showed a unique surface morphology, i.e. large spherically networked particles enabled to enter the soot particles into the hollow surface during the tight contacting the soot and catalyst. Thus, the soot particles are available on both the inner and outer surfaces of the hollow spherical morphology. During the soot oxidation process (shown in Fig. 12), the vacancies (V_{i-s} = inner surface vacancy and V_{o-s} = outer surface vacancy) filled by molecular oxygen in the inner and
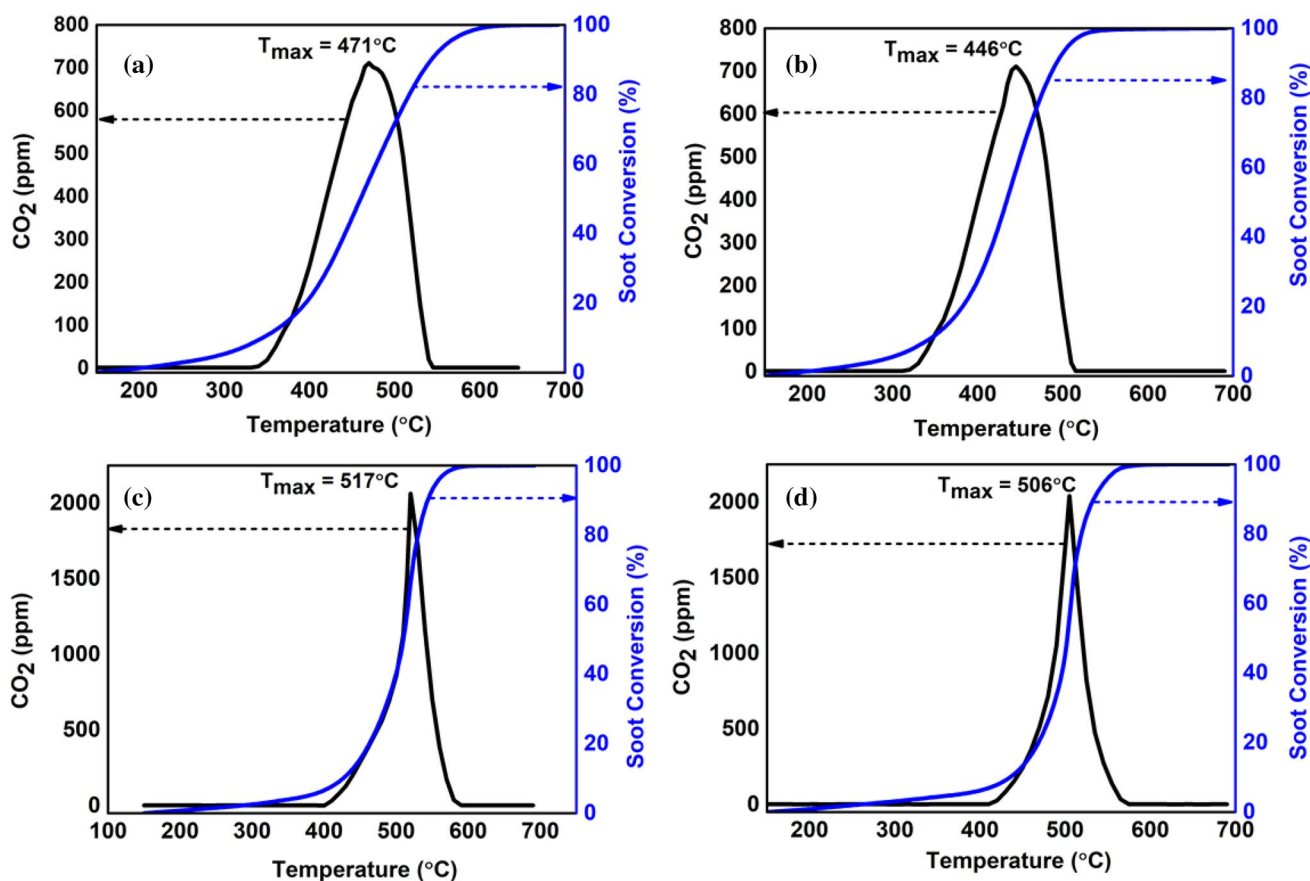
Fig. 11 Soot oxidation and the corresponding CO_2 emissions over as-synthesized samples **a** NC1 **b** NC2 **c** NC3 and **d** NC4

outer surface catalyst particles enable to convert into active oxygen species $\left(O_2^{x-}\right)$ due to the availability of two different cobalt cations (evidenced by Co2p analysis). However, the transition of O_2 to $\left(O_2^{x-}\right)$ occurs slowly in the inner surface of the catalyst than the outer surface, because the molecular oxygen should travel through the voids of the spherical morphology and interact with the surface vacancies and convert into active species, which would delay the oxidation process. Thus, the active oxygen species can able to interact with the outer surface contacted soot particles rapidly than the inner surface soot particles. Similarly, the same soot oxidation mechanism can also be interpreted for the NC2 sample as well. In NC2, the ignition starts at around 360 °C and completes at around 525 °C with a temperature gap of 165 °C. The soot combustion temperatures in NC2 are lower than NC1 because of higher content of Co^{2+} than Co^{3+} (Co^{2+}/ Co^{3+} = 5.13) as well as higher availability of active oxygen species ($O_\beta/(O_\alpha+O_\beta+O_\gamma)$ = 0.587). In addition, NC2 possessed more surface morphological advantages than NC1, because the NC2 sample contains the smaller size spherical networked particles than NC1. Thus, the NC2 sample exhibits a profound oxidation process than NC1 because of the less travel time required for the molecular oxygen to

enter the inner surface through the voids and convert into active species.

On the other hand, NC3/NC4 samples disappeared the network-like morphology upon introducing higher Ce/Cu cation content. It evidences that NC3/NC4 exhibits higher soot oxidation temperatures than NC1/NC2. The samples NC3/NC4 start to ignite at around ~ 450 °C and complete at around ~ 570 °C. Although the soot oxidation temperatures in NC3/NC4 are up-shifted to higher temperatures than NC1/NC2, the temperature gaps of NC3 (125 °C) and NC4 (115 °C) are down-shifted to lower temperatures. This is due to the fact that NC3/NC4 samples exhibit the individually separated particles, which enables interaction of the active oxygen species with the only outer surface contacted soot particles. Thus, the oxidation reaction occurs so rapidly in NC3/NC4 as soon as it starts to ignite. Furthermore, NC3/ NC4 samples exhibit the good content of Co^{2+} cations, which is nearly equal to or more than NC2/NC1 and also exhibited higher mobility of oxygen species. But the soot combustion is shown at a higher temperature because of individually separated particles which limits the oxidation process and also higher content of Ce/Cu cations led to inefficient catalytic property. Thus, the surface morphological
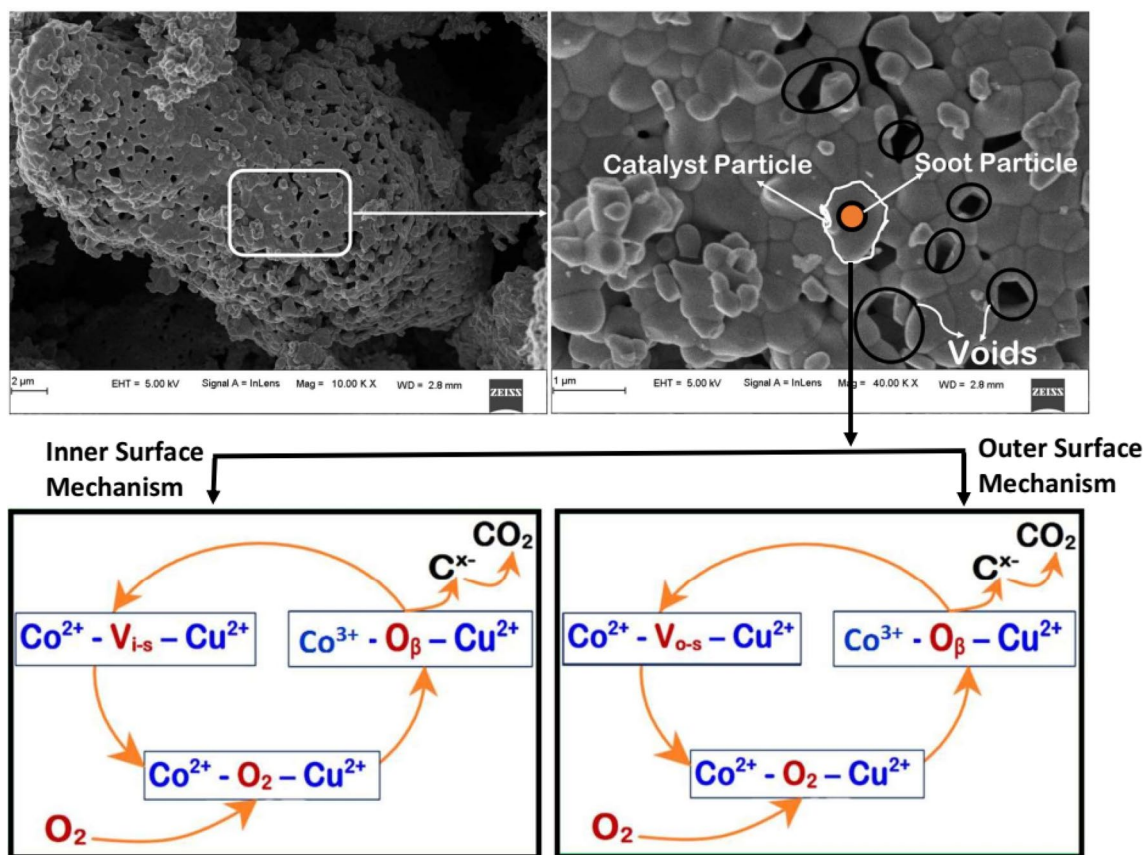
Fig. 12 The demonstration of soot oxidation mechanism over inner and outer catalyst surface

properties also decide the oxidation process along with the surface oxygen species and redox capability of the catalysts.

The samples NC1/NC2 exhibited a higher soot oxidation rate than NC3/NC4 because of surface morphological advantage, particularly forming spherical network morphology with voids. It enables the soot to penetrate through the voids and increases the more contact points with the catalyst. However, increasing the dopant composition beyond the optimum level (NC3/NC4) led to the disappearance of the spherical network and formed the individually separated nanoparticles, promoting fewer contact points with the soot. Thus, the sample NC2 exhibited a much better performing candidate towards soot oxidation activity than other perovskites. It is due to good surface morphology, lower bandgap energy, higher mobility of surface-adsorbed oxygen species, and the good reducible nature of the catalyst.

In addition, the relationship of catalytic soot oxidation with the soot-TPR peak temperatures, amount of surface-adsorbed oxygen species, and the bandgap energy values are established and shown in Fig. 13. For any better performing catalyst, it should possess a lower $T_{50\%}$ value, lower soot-TPR peak temperature, lower bandgap energy, and higher amount of surface-chemisorbed oxygen. Moreover, surface

morphology also plays a crucial role in soot oxidation reactions.

Among the samples, NC1/NC2 shown on the left side of the separated arrow in Fig. 13 Exhibited lower soot-TPR temperature peaks, lower bandgap energy, and excellent spherical networked surface morphology with inner and outer surface contact points promoted the lower soot oxidation temperature. Besides, the amount of surface-adsorbed oxygen species (O_β-species) was shown the highest for the NC2 sample; however, NC1 attributed the least O_β-species. Similarly, NC3/NC4 samples shown on the right side of the separated arrow in Fig. 13 demonstrated higher-temperature soot-TPR peaks and higher bandgap energy as compared with NC1/NC2, which successively promoted the lower catalytic activity. Although NC3/NC4 exhibited a higher amount of O_β-species than NC1, it showed lower catalytic activity because of individually separated particles providing less surface contact with the soot particles and also the substitution of higher content of Ce/Cu content into the perovskite. Among the prepared samples, $T_{50\%}$ of NC2 was found to be 434 °C because of showing lower soot-TPR peak temperature (462 °C), lower bandgap energy (4.21 eV), and a higher amount of active oxygen species. Thus, the perovskite
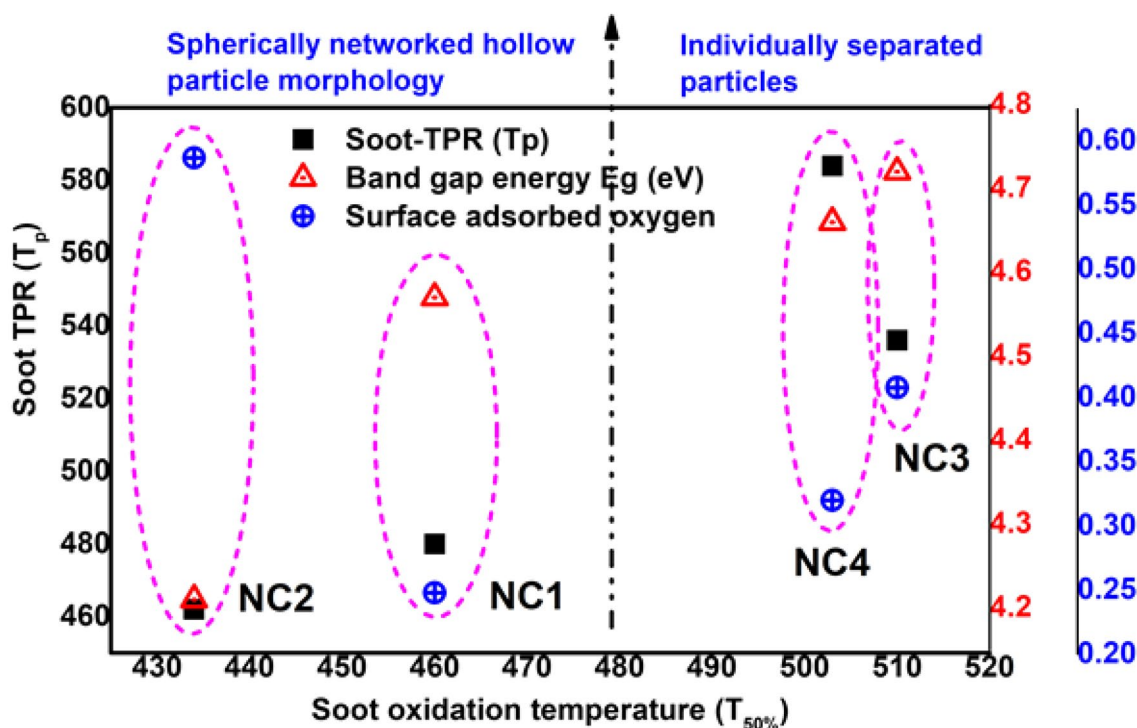
Fig. 13 The relationship of soot-TPR peak/bandgap energy/surface oxygen species with the soot oxidation temperature
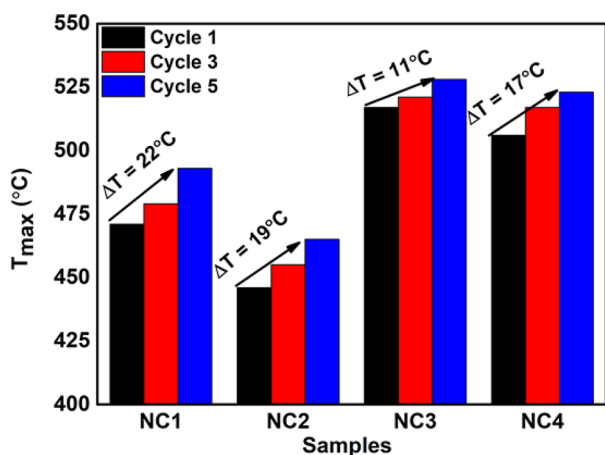

Fig. 14 Reusability studies of as-synthesized perovskites

NC2 exhibited higher catalytic activity as compared with the other perovskites.

The results proved that the perovskite NC2 demonstrated excellent catalytic features; however, the investigation of multiple cycles of soot oxidation reactions helps to understand the behaviour of catalytic stability. Figure 14 depicts the perovskite reusability studies carried under the same experimental conditions. It can be seen from Fig. 14 that there was a rise in maximum soot oxidation temperature of nearly ~ 10 to 20 °C for all the samples. Thus, all the

perovskite samples were catalytically stable even after five cycles of oxidation reactions. It signifies that as-synthesized samples can be reused for multiple cycles with less significant loss of catalytic activity.

Conclusions

In summary, the perovskites $Nd_{1-x}Ce_xCo_{1-y}Cu_yO_3$ ($x = 0$–0.05, $y = 0$–0.1) were successfully synthesized using PVP-assisted sol–gel method. XRD technique reveals that the perovskite samples exhibited an orthorhombic phase. FESEM images showed the spherically networked-like morphology with around 300–500 nm particle sizes with size-ratio factor was more than one, indicating a catalyst surface exhibiting more contact points with the soot. FTIR technique evidenced that upon doping Ce^{4+} and Cu^{2+} into $NdCoO_3$, the stretching vibration of Co–O or Cu–O in BO_6 octahedron at higher wavenumber and bending vibration of O–Co–O or O–Cu–O at lower band was observed in the perovskite structure. Moreover, the perovskites exerted LMCT transitions and inter-band transition in the UV region (210–260 nm) and also observed absorption bands at around ~ 380–600 nm, indicating that the samples are visible radiation responsive. Besides, bandgap energies are also calculated, NC2 remarkably exhibited the least bandgap energy as compared with the others. All the doped samples evidenced

more amount of Co^{2+} cation as compared with NC1. The amount of O_β-species evaluated from O1s are in the order of $NC2 > NC3 > NC4 > NC1$. Thus, the NC2 sample was found to be a higher catalytic activity with $T_{50\%}$ as 434 °C because of exhibiting lower soot-TPR peak temperature (462 °C), lower bandgap energy (4.21 eV), and a higher amount of active oxygen species. Furthermore, the unique surface morphology of the NC2 sample also played a decisive factor for soot oxidation reactions, in another way, the penetration of soot particles in the hollow spherically network morphology in which inner and outer catalyst's surface was utilized for oxidation reactions.

Authors' contributions HP developed the methodology, investigated the experiments, and written the original draft. HD conceptualized, supervised, allocated the resources, and reviewed the manuscript. SK helped in interpretation of analysed data, validated the results, and reviewed the original draft. NK administered the project, allocated the resources, and validated the results. MS helped in formal analysis.

Availability of data and materials The datasets used and/or analysed during the current study are available from the corresponding author on reasonable request.

Declarations

Conflict of interest The authors declare that they have no known competing financial interests or personal relationships that could have appeared to influence the work reported in this paper.

Human or Animal Rights The authors declare that they have no research involving human participants or animals in this work.

References

Adler J (2005) Ceramic diesel particulate filters. Int J Appl Ceram Technol 439:429–439. https://doi.org/10.1111/j.1744-7402.2005.02044.x

Ateia EE, Arman MM, Morsy M (2019) Synthesis, characterization of $NdCoO_3$ perovskite and its uses as humidity sensor. Appl Phys A Mater Sci Process 125:1–9. https://doi.org/10.1007/s00339-019-3168-6

Basu T, Ghosh UC (2013) Nano-structured iron(III)-cerium(IV) mixed oxide: synthesis, characterization and arsenic sorption kinetics in the presence of co-existing ions aiming to apply for high arsenic groundwater treatment. Appl Surf Sci 283:471–481. https://doi.org/10.1016/j.apsusc.2013.06.132

Cui B, Yan S, Xia Y et al (2019) $Cu_xCe_{1-x}O_2$ nanoflakes with improved catalytic activity and thermal stability for diesel soot combustion. Appl Catal A Gen 578:20–29. https://doi.org/10.1016/j.apcata.2019.03.025

Fang S, Wang L, Sun Z et al (2014) Catalytic removal of diesel soot particulates over K and Mg substituted $La_{1-x}K_xCo_{1-y}Mg_yO_3$ perovskite oxides. Catal Commun 49:15–19. https://doi.org/10.1016/j.catcom.2014.01.029

Feng N, Wu Y, Meng J et al (2015) Catalytic combustion of soot over Ce and Co substituted three-dimensionally ordered macroporous $La_{1-x}Ce_xFe_{1-y}Co_yO_3$ perovskite catalysts. RSC Adv 5:91609–91618. https://doi.org/10.1039/c5ra14997e

Feng N, Meng J, Wu Y et al (2016) KNO_3 supported on three-dimensionally ordered macroporous $La_{0.8}Ce_{0.2}Mn_{1-x}Fe_xO_3$ for soot removal. Catal Sci Technol 6:2930–2941. https://doi.org/10.1039/c5cy02025e

Feng N, Chen C, Meng J et al (2017) K-Mn supported on three-dimensionally ordered macroporous $La_{0.8}Ce_{0.2}FeO_3$ catalysts for the catalytic combustion of soot. Appl Surf Sci 399:114–122. https://doi.org/10.1016/j.apsusc.2016.12.066

Getsoian A, Zhai Z, Bell AT (2014) Band-gap energy as a descriptor of catalytic activity for propene oxidation over mixed metal oxide catalysts. J Am Chem Soc 136:13684–13697. https://doi.org/10.1021/ja5051555

Guo X, Meng M, Dai F et al (2013) NOx-assisted soot combustion over dually substituted perovskite catalysts $La_{1-x}K_xCo_{1-y}Pd_yO_{3-\delta}$. Appl Catal B Environ 142–143:278–289. https://doi.org/10.1016/j.apcatb.2013.05.036

Han GH, Lee SH, Seo MG, Lee KY (2020) Effect of polyvinylpyrrolidone (PVP) on palladium catalysts for direct synthesis of hydrogen peroxide from hydrogen and oxygen. RSC Adv 10:19952–19960. https://doi.org/10.1039/d0ra03148h

Koczkur KM, Mourdikoudis S, Polavarapu L, Skrabalak SE (2015) Polyvinylpyrrolidone (PVP) in nanoparticle synthesis. Dalt Trans 44:17883–17905. https://doi.org/10.1039/c5dt02964c

Lee C, Jeon Y, Hata S et al (2016) Three-dimensional arrangements of perovskite-type oxide nano-fiber webs for effective soot oxidation. Appl Catal B Environ 191:157–164. https://doi.org/10.1016/j.apcatb.2016.03.001

Levasseur B, Kaliaguine S (2009) Effects of iron and cerium in $La_{1-y}Ce_yCo_{1-x}Fe_xO_3$ perovskites as catalysts for VOC oxidation. Appl Catal B Environ 88:305–314. https://doi.org/10.1016/j.apcatb.2008.11.007

Li Z, Meng M, Li Q et al (2010) Fe-substituted nanometric $La_{0.9}K_{0.1}Co_xFe_xO_{3-\delta}$ perovskite catalysts used for soot combustion, NOx storage and simultaneous catalytic removal of soot and NO_x. Chem Eng J 164:98–105. https://doi.org/10.1016/j.cej.2010.08.036

Li Z, Meng M, Zha Y et al (2012) Highly efficient multifunctional dually-substituted perovskite catalysts $La_{1-x}K_xCo_{1-y}Cu_yO_{3-\delta}$ used for soot combustion, NO_x storage and simultaneous NOx-soot

removal. Appl Catal B Environ 121–122:65–74. https://doi.org/10.1016/j.apcatb.2012.03.022

Liu J, Zhao Z, Lan J et al (2009) Catalytic combustion of soot over the highly active $(La_{0.9}K_{0.1}CoO_3)x/nmCeO_2$ catalysts. J Phys Chem C 113:17114–17123. https://doi.org/10.1021/jp9056303

Liu S, Wu X, Liu W et al (2016) Soot oxidation over CeO_2 and Ag/CeO_2: factors determining the catalyst activity and stability during reaction. J Catal 337:188–198. https://doi.org/10.1016/j.jcat.2016.01.019

Liu G, Wang H, Feng N et al (2019) Construction of substrate-dependent 3D structured MnO_2 catalysts for diesel soot elimination. Appl Surf Sci 484:197–208. https://doi.org/10.1016/j.apsusc.2019.04.090

Mishra A, Prasad R (2014) Preparation and application of perovskite catalysts for diesel soot emissions control: An overview. Catal Rev Sci Eng 56:57–81. https://doi.org/10.1080/01614940.2014.866438

Murugan B, Ramaswamy AV, Srinivas D et al (2005) Nature of manganese species in $Ce_{1-x}Mn_xO_{2-\delta}$ solid solutions synthesized by the solution combustion route. Chem Mater 17:3983–3993. https://doi.org/10.1021/cm050401j

Piumetti M, van der Linden B, Makkee M et al (2016) Contact dynamics for a solid-solid reaction mediated by gas-phase oxygen: study on the soot oxidation over ceria-based catalysts. Appl Catal B Environ 199:96–107. https://doi.org/10.1016/j.apcatb.2016.06.006

Royer S, Duprez D, Can F et al (2014) Perovskites as substitutes of noble metals for heterogeneous catalysis: dream or reality. Chem Rev 114:10292–10368. https://doi.org/10.1021/cr500032a

Safo IA, Werheid M, Dosche C, Oezaslan M (2019) The role of poly-vinylpyrrolidone (PVP) as a capping and structure-directing agent in the formation of Pt nanocubes. Nanoscale Adv 1:3095–3106. https://doi.org/10.1039/c9na00186g

Schön A, Dacquin J-P, Dujardin C, Granger P (2017) Catalytic activity and thermal stability of $LaFe_{1-x}Cu_xO_3$ and La_2CuO_4 perovskite solids in three-way-catalysis. Top Catal 60:300–306. https://doi.org/10.1007/s11244-016-0615-x

Stanmore BR, Brilhac JF, Gilot P (2001) The oxidation of soot: a review of experiments, mechanisms and models. Carbon N Y 39:2247–2268. https://doi.org/10.1016/S0008-6223(01)00109-9

Sun J, Zhao Z, Li Y et al (2020) Synthesis and catalytic performance of macroporous $La_{1-x}Ce_xCoO_3$ perovskite oxide catalysts with high oxygen mobility for catalytic combustion of soot. J Rare Earths 38:584–593. https://doi.org/10.1016/j.jre.2019.05.014

Tsai YC, Huy NN, Tsang DCW, Lin KYA (2020) Metal organic framework-derived 3D nanostructured cobalt oxide as an effective catalyst for soot oxidation. J Colloid Interface Sci 561:83–92. https://doi.org/10.1016/j.jcis.2019.11.004

Uppara HP, Dasari H, Singh SK et al (2019) Effect of copper doping over $GdFeO_3$ perovskite on soot oxidation activity. Catal Lett 149:3097–3110. https://doi.org/10.1007/s10562-019-02843-2

Uppara HP, Pasuparthy JS, Pradhan S et al (2020) The comparative experimental investigations of $SrMn(Co^{3+}/Co^{2+})O_{3\pm\delta}$ and $SrMn(Cu^{2+})O_{3\pm\delta}$ perovskites towards soot oxidation activity. Mol Catal 482:110665. https://doi.org/10.1016/j.mcat.2019.110665

Uppara HP, Singh SK, Labhsetwar NK et al (2021) The catalytic activity of Ce-Hf, Ce-Hf-Mg mixed oxides and RuO_2/HfO_2 deposited on CeO_2: role of superoxide/peroxide in soot oxidation reaction. Korean J Chem Eng 38:1–13. https://doi.org/10.1007/s11814-021-0805-5

Urán L, Gallego J, Bailón-García E et al (2020) Isotopic study of the $La_{0.7}Ag_{0.3}MnO_{\delta\le3}$ perovskite-catalyzed soot oxidation in presence of NO. Appl Catal A Gen 599:117611. https://doi.org/10.1016/j.apcata.2020.117611

Venkataswamy P, Jampaiah D, Mukherjee D, Reddy BM (2019) CuO/Zn-CeO_2 nanocomposite as an efficient catalyst for enhanced diesel soot oxidation. Emiss Control Sci Technol 5:328–341. https://doi.org/10.1007/s40825-019-00137-y

Wang H, Zhao Z, Liang P et al (2008) Highly active $La_{1-x}K_xCoO_3$ perovskite-type complex oxide catalysts for the simultaneous removal of diesel soot and nitrogen oxides under loose contact conditions. Catal Lett 124:91–99. https://doi.org/10.1007/s10562-008-9429-1

Wang K, Qian L, Zhang L et al (2010) Simultaneous removal of NOx and soot particulates over $La_{0.7}Ag_{0.3}MnO_3$ perovskite oxide catalysts. Catal Today 158:423–426. https://doi.org/10.1016/j.cattod.2010.06.001

Wang H, Liu J, Zhao Z et al (2012) Comparative study of nanometric Co-, Mn- and Fe-based perovskite-type complex oxide catalysts for the simultaneous elimination of soot and NO_x from diesel engine exhaust. Catal Today 184:288–300. https://doi.org/10.1016/j.cattod.2012.01.005

Wang R, Ye C, Wang H, Jiang F (2020) Z-scheme $LaCoO_3/g$-C_3N_4 for efficient full-spectrum light-simulated solar photocatalytic hydrogen generation. ACS Omega 5:30373–30382. https://doi.org/10.1021/acsomega.0c03318

Xiong J, Wu K, Yang J et al (2021) The effect of existence states of PdO_x supported by Co_3O_4 nanoplatelets on catalytic oxidation of methane. Appl Surf Sci 539:148211. https://doi.org/10.1016/j.apsusc.2020.148211

Zhai G, Wang J, Chen Z et al (2019) Highly enhanced soot oxidation activity over 3DOM Co_3O_4-CeO_2 catalysts by synergistic promoting effect. J Hazard Mater 363:214–226. https://doi.org/10.1016/j.jhazmat.2018.08.065